Nitrogen fixation in pulsed microwave discharge studied by infrared absorption combined with modelling

Nitrogen fixation in pulsed microwave discharge studied by infrared absorption combined with modelling

Omid Samadi Bahnamiri[1,†], Claudia Verheyen[1,2], Rony Snyders[1,3], Annemie Bogaerts[2] and Nikolay Britun[1,4]

[1]Chimie des Interactions Plasma-Surface (ChIPS), CIRMAP, Universit de Mons, 23 Place du Parc, 7000 Mons, Belgium
[2]Research group PLASMANT, Department of Chemistry, University of Antwerp, Universiteitsplein 1, BE-2610 Antwerp, Belgium
[3]Materia Nova Research Center, Parc Initialis, 7000 Mons, Belgium
[4]Pressent Address: Center for Low-temperature Plasma Sciences, Nagoya University, Chikusa-ku, Nagoya, 464-8603, Japan

† corresponding author:

E-mail: omid.samadibahnamiri@umons.ac.be

Abstract.

A pulsed microwave surfaguide discharge operating at 2.45 GHz was used for the conversion of molecular nitrogen into valuable compounds in several gas mixtures: N_2:O_2, N_2:O_2:CO_2 and N_2:CO_2. The ro-vibrational absorption bands of the molecular species were monitored by a fourier transform infrared apparatus in the post-discharge region in order to evaluate the relative number density of species, specifically NO production. The effects of specific energy input, pulse frequency, gas flow fraction, gas admixture and gas flow rate were studied for better understanding and optimization of the NO production yield and the corresponding energy cost. By both the experiment and modelling, a highest NO yield is obtained at N_2:O_2 (1:1) gas ratio in N_2:O_2 mixture. The NO yield reveals a small growth followed by saturation when pulse repetition frequency increases. The energy efficiency start decreasing after the energy input reaches about 5 eV/molec, whereas the NO yield rises steadily at the same time. The lowest energy cost of about 8 MJ/mol corresponding to the yield and the energy efficiency of about 7% and 1% are found, respectively, in an optimum discharge condition in our case.

Keywords:

Nitrogen fixation, pulsed microwave discharge, FTIR spectroscopy, discharge modelling, vibrational excitation, NO yield, energy cost

1. Introduction

Nitrogen comprises a significant fraction of the Earth's atmosphere playing a critical role in regulating disease resistance and growth of plants in the environment [1, 2]. However, this abundant element is chemically inert and hardly accessible to the majority of living organisms because of its extremely strong triple bond formed as a result of a very stable electronic configuration. Numerous attempts have been made to artificially convert nitrogen molecules into N-containing compounds, such as NO_x, NH_3, etc, in a process known as nitrogen fixation [3, 4]. For industrial nitrogen fixation, the Birkeland-Eyde [5] and Haber-Bosch (H-B) [6] processes represent two of the most revolutionary industrial approaches to produce NO and NH_3, respectively. The B-E process uses an electrical arc discharge to generate thermal plasma from air at high temperatures, but it has low energy efficiency. On the other hand, the energy efficiency of thermal plasma cannot compete with the H-B process. The resulting chain of fertilizers production involving the H-B process is quite inefficient, resulting in a drastic perturbation to the worldwide geochemical N cycle. This process consumes almost 1-2% of the world's total energy supply emitting more than 300 million tons of carbon dioxide annually [7]. More importantly, the high temperature and extreme pressure required are the main obstacles of the H-B process for nitrogen fertilizer production [8]. Therefore, alternative processes are of high importance to be efficient for this approach.

Nowadays, *plasma-assisted* nitrogen fixation is gaining more interest and is considered as a very promising alternative to the well-established but environmentally harmful H-B process [9]. Non-thermal plasmas (NTPs) provide an opportunity of producing N-containing products by breaking the N_2 bond into radicals [10]. NTP has significantly lower theoretical limit of energy cost, which is 2.5 times lower than the H-B process limit, for N_2 dissociation [11]. The reason for this is the presence of highly energetic electrons in NTPs producing highly reactive species and enabling thermodynamically unfavorable reactions [12].

Microwave (MW) discharges, in particular, those based on surface wave launchers where plasma is sustained by surface electromagnetic waves [13,14], have recently attracted much attention for chemical synthesis. The major advantage of these discharges is a high degree of non-equilibrium at low pressure [15, 16]. Based on previous studies [17–21], in these discharges a significant vibrational excitation of species, specifically N_2, at relatively low gas temperature can be achieved. The vibrationally excited N_2 molecules can populate higher vibrational energy levels through a stepwise vibrational-vibrational (V-V) quanta exchange, sometimes called "vibrational ladder climbing" [22]. Excited molecules can relax back to lower vibrational levels via vibrational-translational (V-T) relaxation, afterwards [23]. This is an unfavorable process because the vibrational energy required to overcome the dissociation energy barrier is lost to gas heating. One of the effective ways to prevent the gas temperature from rise is discharge power modulation, i.e. working in pulsed regime with a certain repetition rate [24,25]. In pulsed MW discharges, the gas temperature decreases rather rapidly between pulses while the vibrational temperature reduces more slower as reported by Jivotov *et al.* [26]. The power pulsing can suppress the unfavorable V-T relaxation achieving a maximal vibrational excitation in nitrogen MW discharges, as recently studied by Van Alphen *et al.* [27] by modelling and experiments. This important property makes MW plasmas very interesting for energy-efficient vibrational excitation.

Among the other advantages, MW plasmas are also friendly to in-situ optical diagnostics. Optical emission spectroscopy (OES) [28–30], laser induced fluorescence (LIF) [31–33], Fourier Transform Infrared (FTIR) spectroscopy [34, 35], and other methods can be applied non-intrusively, i.e. without perturbing the plasma kinetics, thus allowing a direct understanding of plasma-chemical processes. In particular, the latter technique allows selective identification of the neutral species formed in the plasma and determination of their chemical structure by their infrared absorption at specific spectral positions, giving complementary information about the IR-active bonding types [36, 37]. Moreover, quantitative results on the ground state density of the relevant plasma radicals can also be obtained by FTIR [38, 39].

To date, several different plasma types, such as direct current (DC) discharges [40, 41], dielectric barrier discharges (DBDs) [42,43], radio-frequency (RF) discharges [44], gliding arc plasmas (GAPs) [3, 45–47] and MW discharges [27, 48] were investigated for nitrogen fixation. The most promising results in terms of yield and energy cost for NO_x production are obtained so far in MW discharges and GAPs. Asisov *et al.* [49] reported a microwave (MW) reactor at low pressure, resulting in an energy cost of 0.29 MJ/mol for a NO_x yield of 14%. Recently, Patil *et al.* [18] investigated a milli-scale GAP reactor with a 2% NO_x yield and 2.8 MJ/mol energy cost at atmospheric pressure. In spite of the strong efforts aiming in NO_x synthesis in high pressure discharges [42, 46], it still results in rather low NO_x yields and poor efficiencies which scientists have yet to overcome. Achieving better NO_x yield with lower energy cost is of particular interest in our case. One of the best potential candidates to respond to these challenges, low-pressure pulsed MW discharges, remain particularly unexplored for nitrogen fixation, but at the same time they could provide better

insights in NO_x formation.

In our work we used a pulsed discharge based on surface wave launchers operating at 2.45 GHz in low pressure (0.5-15 Torr). The effects of plasma pulse parameters, energy input, gas flow fraction, gas pressure and gas admixture were analyzed by in-situ FTIR spectroscopy of the vibrational absorption bands of the relevant molecules, specifically NO. In addition, particular attention was devoted to investigate the evolutions of the NO yield, energy efficiency and energy cost at different discharge conditions. The present paper is organized as follows: after a brief theoretical explanation of nitrogen fixation process, a short description of the experimental setup and diagnostic methods are given. The obtained results are then presented being accompanied by corresponding discussions. Finally, concise conclusions summarize the work.

2. Theoretical notations

The overall reaction for the synthesis of nitrogen oxide in N_2-O_2 gas mixture is typically presented simply as:

$$N_2 + O_2 \longrightarrow 2NO \tag{1}$$

The standard enthalpy of NO formation, $E_{th}(NO)$, is given below [9]:

$$E_{th}(NO) = 90.4\ kJ/mol \simeq 0.93\ eV/molec \tag{2}$$

In non-thermal plasmas, NO formation from N_2-O_2 mixture is initiated through the electron impact dissociation and excitation of N_2 and O_2 molecules resulting in generation of N atoms, O atoms and various excited states of N_2 and O_2. These chemical reaction pathways can be described as follows [26]:

$$e^- + N_2[v=0] \longrightarrow e^- + N_2[v>0] \tag{3}$$

$$e^- + O_2[v=0] \longrightarrow e^- + O_2[v>0] \longrightarrow e^- + O + O \tag{4}$$

Where v indicates the vibrational state. The vibrational excitation of N_2 lowers the bond strength of the molecule and allows for NO generation in non-thermal conditions through reactions with atomic oxygen (see reaction (5) below). Additional NO generation can also be achieved by a secondary exothermic process through reaction (6) [50]:

$$N_2(^1\Sigma_g^+, v) + O(^3P) \longrightarrow NO(^2\Pi) + N(^4S), \quad E_a \simeq E_{th} \simeq 3\ eV/molec \tag{5}$$

$$N(^4S) + O_2(^3\Sigma, v) \longrightarrow NO(^2\Pi) + O(^3P), \quad E_a \simeq 0.3\ eV/molec, E_{th} \simeq -1\ eV/molec \tag{6}$$

Reaction (5) is of importance for the NO production in discharges with relatively high vibrational excitation of N_2 molecules. This pathway is known as the Zeldovich mechanism stimulated by non-equilibrium vibrational excitation of nitrogen molecules [10, 17].

The specific energy input, SEI, is given by the ratio of the discharge power (P) to the gas flow rate (F = $[N_2]$+$[O_2]$) through the discharge volume and it can be expressed in eV per molecule as shown below [51]:

$$SEI \simeq 0.014\ \frac{P(W)}{F(L\ min^{-1})}\ [\frac{eV}{molec}] \tag{7}$$

Another parameter, characterizing the dissociation, is the NO yield expressed as:

$$Yield_{NO} = \frac{1}{2}\frac{moles\ of\ [NO]\ produced}{moles\ of\ [F]\ in\ feed} \tag{8}$$

Traditionally, by using the discharge power and measured NO concentration, the energy cost (EC) and energy efficiency (η) are calculated by equation (9) and (10), respectively, as given below [10]:

$$EC = \frac{P(W)}{NO\ produced\ (\frac{mol}{s})}\ \frac{1}{10^6(\frac{J}{MJ})}\ [\frac{MJ}{mol}] \tag{9}$$

$$\eta = \frac{E_{th}(NO)}{EC} \tag{10}$$

Where EC is energy expended per unit of reactive N (only NO in our case) and expressed in MJ/mol.

3. Experimental setup and diagnostic methods

3.1. The microwave plasma source. The experimental setup of pulsed MW plasma reactor used for nitrogen fixation process is schematically shown in Fig. 1. The reactor represents a surfaguide plasma source operating at 2.45 GHz and working in the pulsed regime triggered by an external delay generator. In our work the discharge was sustained inside a quartz tube with a 14mm inner diameter and about 31cm length, surrounded by a polycarbonate tube. Meanwhile, silicone oil circulating between these tubes was used for cooling purpose. The oil temperature was fixed at about 10°C. The polycarbonate tube was also surrounded by a grounded aluminium grid to prevent MW radiation leak. The gas inlet is placed at the top of the tube and regulated by electronic mass flow controllers. The microwave radiation was fed into the waveguide, connected to a manually tuned three-stub system and terminated by a movable plunger (matching) in order to minimize the reflected power. Three power values were controlled in the power supply: incident, reflected, and total power. The MW power was also modulated by square pulses with duty cycle adjustment. The main parameters of the described microwave system are also listed in Table 1. Further descriptions of the microwave system

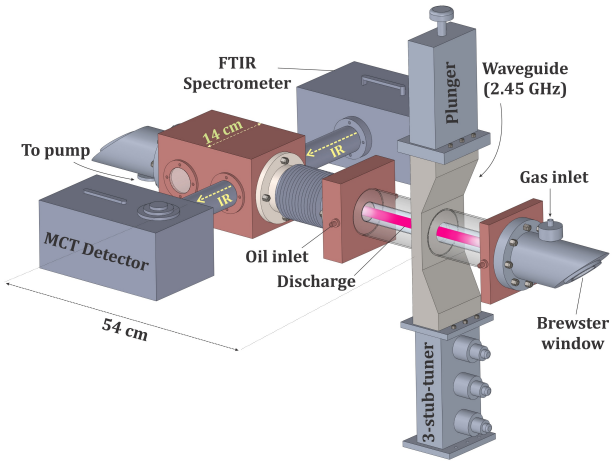

Figure 1. 3D schematic view of the microwave plasma source used in this work. The discharge is generated in the quartz tube for N_2:O_2 (1:1) gas mixture. The mean applied power is 0.7 kW with the pulse repetition rate of 0.5 kHz.

Table 1. Main parameters of the microwave surfaguide discharge used in this study.

Parameter	Value
MW Frequency	2.45 GHz
Mean applied power range	0.5-0.9 kW
Reflected power value[a]	∼5%
Range of pulse repetition rate	0.1-2.0 kHz
Quartz tube inner diameter	14 mm
Polycarbonate tube inner diameter	32 mm
Quartz tube length	31 cm
Post-discharge chamber size	15×15×10 cm^3
Base pressure[b]	$< 10^{-1}$ Torr
Pressure range	0.5-15 Torr
Typical gases used	N_2, O_2, CO_2
Gas flow rate range	100-5000 sccm
Cooling oil temperature	10°C

[a] Controlled manually.
[b] Pressure inside the tube without adding any gas.

can be found in [52, 53]. Measurements in gas mixtures of N_2:O_2, N_2:O_2:CO_2 and N_2:CO_2 were performed at different flow rates and microwave parameters, such as power and pulse repetition rate. The main features of the microwave system are horizontal position and movable post-discharge in order to implement the diagnostic apparata, specifically the FTIR spectrometer.

3.2. The FTIR system. In this study, a custom-design Vertex-80v-based FTIR system (Brucker) with an external mercury-cadmium-telluride (MCT) IR detector unit, pumped internal parts and IR beam path has been used, as shown in Fig. 2. The standard spectrometer configuration is designed for measurements in mid-IR region between 350-5000 cm^{-1}. Optionally, the spectral range can be expanded by exchanging the installed mid-IR components, e.g., source, detector and beamsplitter, for the corresponding optical components allowing measurement in either far- or near-IR region (see Table 2). The IR beam is passed through the ZnSe windows placed in the walls of the post-discharge chamber, and then terminated to the MCT detector. The detector is cooled down by liquid nitrogen. The distance from the collimator to the detector was kept about 70 cm, while the absorbance length was about 14 cm in our case. To minimize the influence of the water and CO_2 atmospheric absorption bands, the whole absorption path in the FTIR system was pumped. The FTIR system has been controlled by the OPUS 7.5 spectroscopy software. The spectral resolution of the measurements was set to 0.08 cm^{-1}, and 30 scans were averaged to acquire each spectrum. The interferometer was configured with a KBr beamsplitter and MCT detector to record the 1300-2500 cm^{-1} region. The spectra were measured after 5 min of stable discharge for each experimental condition. For the quantitative analysis of the acquired molecular absorption bands, a spectral calibration in the spectral range of interest (using commercially available NO gas) has been performed.

The concentration of the various species observed in the post-discharge region is evaluated using Beer-Lambert law [33, 54]. This is the fundamental law of quantitative absorption spectroscopy and is derived as below:

$$I(\sigma) = I_0 \exp[-\varepsilon(\sigma)cl] \tag{11}$$

Where $\varepsilon(\sigma)$ is molar extinction coefficient and has the units of (concentration × length)$^{-1}$, I(σ) is the absorbed intensity (after passing the gas sample), $I_0(\sigma)$ is the intensity of the reference source, c is concentration of absorbers in the gas, and l is optical path length. Transmittance of any sample at the wavenumber σ, T(σ), is given by the ratio of I(σ) and $I_0(\sigma)$:

$$T(\sigma) = \frac{I(\sigma)}{I_0(\sigma)} \tag{12}$$

Absorbance of the sample at σ, A(σ), is defined by the base 10 logarithm of 1/T(σ):

$$A(\sigma) = log_{10}[\frac{1}{T(\sigma)}] \tag{13}$$

The absorbance of any component is proportional to its concentration in the sample. In this paper, the observed NO absorption band was quantified by its fundamental IR transition about 1960-1770 cm^{-1}, whereas NO_2 is not formed in our case. A known NO concentration has been introduced in the discharge volume (without switching plasma on) and measured by FTIR system for

Table 2. Main spectroscopic parameters of the infrared absorption and the optical emission methods used in this study.

Parameter	Value
FTIR diagnostics	
IR Source	Mid-IR
Beamsplitter	KBr
Detector	MCT mid band
Detector cooling	Liquid nitrogen
Sample compartment	not used
Spectral resolution	0.08 cm^{-1}
Laser radiation type	HeNe
Compressed-air supply	1-2 bar
IR beam diameter[a]	5 or 40 mm
Interferometer	Michelson
Distance[b]	70 cm
Aperture	1.5 mm
Optical emission diagnostics	
Monochromator	Andor SR750
Grating	1800 g/mm, 2400 g/mm
Resolution	23 pm
Detector used	Andor iStar740 ICCD

[a] It can be either focalized or collimated beam.
[b] Free distance between IR output and detector.

the calibration purpose. The obtained values were then compared to the experimentally measured absorbances in the presence of plasma in order to deduce the absolute NO density values for each studied plasma condition. Note that a typical error of our measurements is estimated about 5-10%.

3.3. Optical emission spectroscopy. Spectral lines from a second positive system of the N_2 $C^3\Pi_u \longrightarrow B^3\Pi_g$ transition have been used for both vibrational (T_{vibr}) and rotational (T_{rot}) temperature determinations. The details related to the OES are also listed in Table 2. The vibrational bands sequence from N_2(C,v-1 B,v), N_2(C,v-2 B,v), N_2(C,v-3 B,v) and N_2(C,v-4 B,v) were used for T_{vibr} determination in the N_2(C) excited state. For the gas temperature (T_{gas}) calculations, rotational temperature of the excited N_2(C, v=0) state has been determined, using rotational emission band at 380.5nm. The rotational spectra were acquired with about 23pm spectral resolution. T_{gas} is assumed to equal T_{rot} in our case. The Boltzmann plot approach for the rotational lines with numbers from J=18 through 29^{th} has been used. A possible two-slope band shape has not been investigated since the spectral resolution was not enough to access the rotational lines with lower numbers.

4. Model description

In this work the experimental data has been accompanied by modelling for cross-checking the data reliability as well as for a deeper understanding of the found effects. The model concept as well as the chemistry set used are briefly explained in this section

4.1. Plasma model. A zero-dimensional model of a plug-flow [55] reactor was chosen, where a volume element was followed along the discharge tube. By using this approach time-dependence of the model can be converted to axial dependence using the velocity of the considered gas volume. The zero-dimensionality assumes a homogeneity throughout the volume element by transport phenomena like convection and neglects diffusion along the reactor axis. The calculations were performed by the Fortran 90 plasma kinetics model, ZDPlasKin (Zero-Dimensional Plasma Kinetics solver) [55]. The detailed description defining the model can be found in the Appendix.

4.2. The chemistry set. The chemistry set considered in this research is adapted from the N_2-O_2 set developed by the modelling group PLASMANT, as described elsewhere [47]. It contains 82 species (as given in Table 3) and 4615 reactions, including N_2 and O_2 ground state molecules, N and O atoms, vibrationally excited N_2 and O_2 molecules, various N and O ions, and several electronically excited N_2 and O_2. It deals with the extended N_2 vibrational kinetics, including 21 vibrational levels of N_2 and V-V and V-T reactions for N_2-N_2 and N_2-O_2. The latter O_2 has 15 vibrational levels included in the set. Vibrational kinetics are of great importance to set since they allow taking into account vibrational ladder climbing and verify the importance of this process for NO formation in MW discharges.

5. Results and discussions

In this section, the nitrogen conversion results in the MW system are presented starting from the IR absorption spectra and finishing by the effects of specific energy input, plasma pulse parameters, gas flow rate, gas flow fraction and gas admixture affecting NO production.

5.1. The absorption spectra. Typical FTIR spectra of the neutral long-living reactive species generated in the MW reactor at a SEI of 9.75 eV/molec and gas flow rate of 1 slm are shown in Fig. 3. Several absorption bands corresponding to NO, CO and CO_2 molecules are typically observed, as given in Table 4. In N_2:O_2 (1:1) mixture, only NO band is detected,

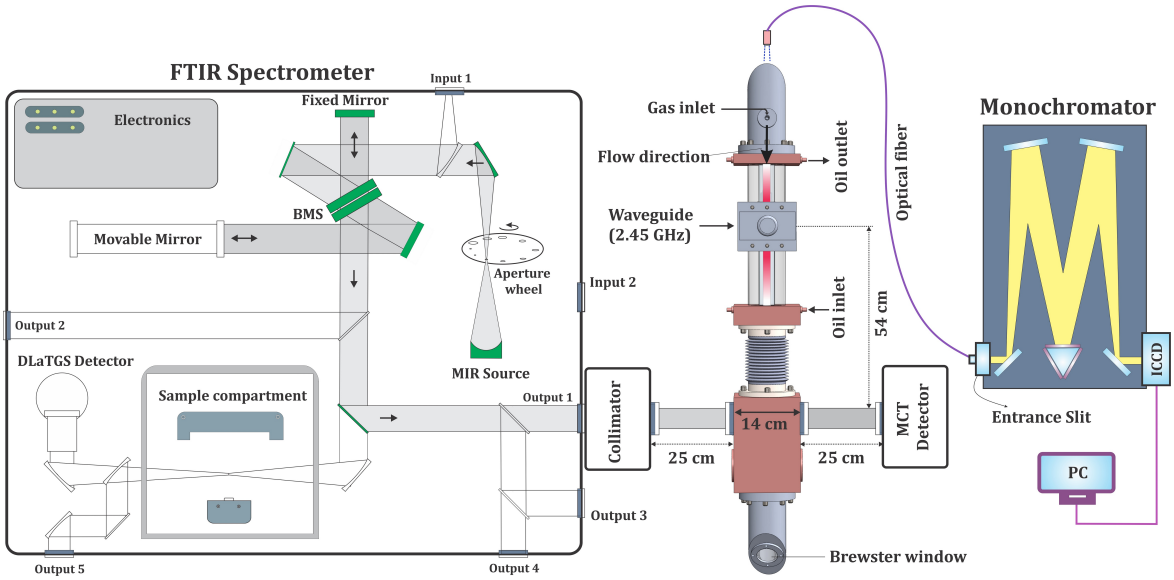

Figure 2. Schematic representation of the FTIR layout, the monochromator and ICCD detector as well as the MW plasma source used in this study. All FTIR sections including optical bench and sample compartments, collimator, MCT and DLaTGS detectors are pumped. The internal sample compartment and DLaTGS detector were not used in this study.

Table 3. Species included in the model for the N_2-O_2 MW plasma.

Ground state N-species
N_2, N
Vibrationally excited N_2 molecules
$N_2(X^1\Sigma_g^+, v = 1-24)$
Electronically excited N_2 and N
$N_2(A^3\Sigma_u^+), N_2(B^3\Pi_g), N_2(C^3\Pi_u), N_2(a'^1\Sigma_u^-), N(^2D), N(^2P)$
N-ions
N_2^+, N^+, N_3^+, N_4^+
Ground state O-species
O_2, O, O_3
Vibrationally excited O_2 molecules
$O_2(X^3\Sigma, v = 1-15)$
Electronically excited O_2 and O
$O_2(a^1\Delta), O_2(b^1\Sigma^+), O_2(A^3\Sigma^+, C^3\Delta, c^1\Sigma^-), O(^1D), O(^1S)$
O-ions
$O_2^+, O_2^-, O^+, O^-, O_3^-, O_4^+, O_4^-$
N,O-combined species
$N_2O, N_2O_3, N_2O_4, N_2O_5, NO, NO_2, NO_3$ $N_2O^+, N_2O^-, NO_2^+, NO_2^-, O_3^-, NO^+, NO^-, O_2^+(N_2)$

whereas CO band is clearly detectable in presence of CO_2 gas. This figure, however, also shows that CO_2 admixture has an adverse effect on the NO formation so that it decreases upon adding CO_2 gas to the mixture. Detailed description is given in section 5.4.2.

The measured NO absorption band is attributed to fundamental vibrational transition in ground electronic states, recorded in spectral interval 1960-1770 cm^{-1} (see inset in Fig. 3). Indeed, two infrared transitions of $X^2\Pi_{1/2}(\nu{=}1) \leftarrow X^2\Pi_{1/2}(\nu{=}0)$ and $X^2\Pi_{3/2}(\nu{=}1) \leftarrow X^2\Pi_{3/2}(\nu{=}0)$ are observed in our case at 1876.2 and 1875.8 as bandheads, respectively [56–58]. These transitions also have a good agreement with HITRAN database [59]. The $^2\Pi$ ground electronic state of NO is an example of Hunds case (a) of angular momentum coupling. This results in the appearance of two sets of rotational levels denoted by $^2\Pi_{1/2}$ and $^2\Pi_{3/2}$ subbands. The 1←0 vibrational band comprises two allowed subbands which are slightly displaced in frequency due to the change in the spin-orbit coupling parameter with vibrational state. Each rotational level is further splitted by two components as a result of Λ-type doubling, which also results in absorption line splittings [58].

5.2. Influence of specific energy input and gas flow rate.

5.2.1. Specific energy input effect. The evolution of the NO yield and energy efficiency was examined as a function of specific energy input (SEI) in N_2:O_2 (1:1) case. Due to the discharge power limitations, the final SEI range has been tailored by a combination of three datasets taken at different flow rates; 1.0, 1.8 and 2.6 slm resulting in the total range of 2.5-13 eV/molec. The

Table 4. Assignments of the absorption bands monitored by FTIR.

Species	Region covered (cm^{-1})	Transitions	Strength	Ref
NO_2	1650-1580	-	not detected	
NO	1960-1770	$X^2\Pi_{1/2}(\nu{=}1) \leftarrow X^2\Pi_{1/2}(\nu{=}0)$, $X^2\Pi_{3/2}(\nu{=}1) \leftarrow X^2\Pi_{3/2}(\nu{=}0)$	strong	[56–58]
CO	2200-2054	$X^1\Sigma_g^+(\nu{=}1) \leftarrow X^1\Sigma_g^+(\nu{=}0)$	strong	[60, 61]
N_2O	2250-2180	-	not detected	
CO_2	2370-2280	$X^1\Sigma_u^+(\nu{=}001) \leftarrow X^1\Sigma_u^+(\nu{=}000)$	strong	[62]

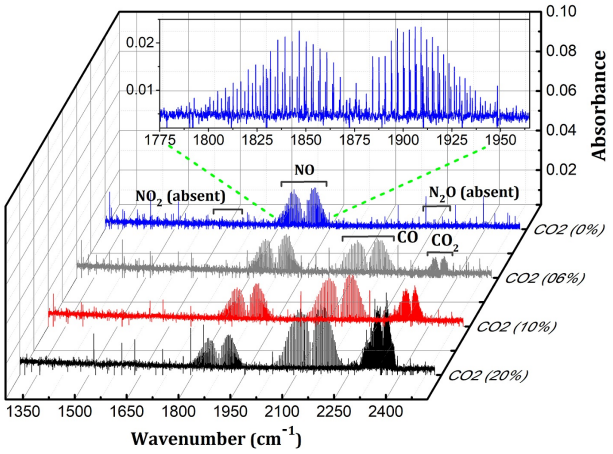

Figure 3. FTIR spectra of N_2:O_2 (1:1) with 0%, 6%, 10% and 20% CO_2 addition at fixed gas flow rate of 1 slm detected in the post-discharge chamber. The observed NO absorption band is considered as the range of interest for quantification purpose.

SEI has been controlled by changing the incident power at fixed gas flow rate for each condition. We can clearly see the continuous growth of the yield, as SEI increases from Fig. 4, whereas the efficiency is showing maximum (energy cost - minimum) at about 4 eV/molec.

The energy efficiency starts decreasing at SEI $>$ 5 eV/molec, whereas the NO yield rises steadily for the same conditions, as represented in Fig. 4(a). The observed trend can be related to a continuous increase in vibrational excitation of N_2 (see reaction (3) above) at higher energy inputs. It should be mentioned that higher SEI could also provide other processes with higher energy threshold (electronic excitation, dissociation, etc). The vibrationally excited N_2 molecules can stepwisely populate higher vibrational energy levels leading to enhanced N_2 dissociation, as verified by additional measurements of $N_2(C)$ vibrational temperature (see Fig. 4(c)). Higher SEI results in the enhanced production of N- and O- reactive species, primarily as a result of the increase in electron (and thus vibrational) excitation. Further on, these reactive species can then combine, resulting in higher NO production. The O atoms produced by electron impact dissociation of O_2, reaction (4), can react with vibrationally excited N_2 to form NO (see reaction (5)). The N atoms formed in this process can participate in a secondary reaction with O_2 creating another NO molecule (see reaction (6)) [3]. It is worth mentioning the yield-gas flow dependence is slowly changing, so the jumps are almost negligible. The importance of the vibrationally excited N_2 for energy-efficient NO formation is discussed separately in section 5.4.1.

The minimum in the energy cost was obtained at relatively low values of SEI and flow rate of 2.6 slm, as shown in Fig. 4(b). The lower energy cost was also found at pulse repetition rate of 0.5 kHz which will be discussed separately below.

5.2.2. Gas flow rate effect. In order to determine the influence of the flow rate on the NO yield, as well as on the corresponding energy cost and energy efficiency, the experiments in gas mixture of N_2:O_2 (1:1) were performed. The data were recorded at a mean power of 0.7 and 0.9 kW at a pulse repetition rate of 0.5 kHz. Note that an increase in gas flow rate is associated with the increase of the discharge pressure in our case. We found that the NO yield decreases from about 12% to about 2.5% by an increase in the gas flow rate from 0.5 to 5 slm at 0.9 kW, as shown in Fig. 5(a). At 0.7 kW, the yield values are similarly reduced from around 10% to around 1.5%.

This fact can be interpreted as follows: the gas flow increase may cause certain drop in electron temperature in the discharge, as a result of higher collision rate between electrons and heavy particles in plasma [15]. Thus, the energy transferred from the electrons to the gas causes an increase in the gas temperature by lowering the electron temperature. Besides, a higher pressure facilitates the V-T relaxation processes when the vibrational energy is transferred to gas heating [23]. As a result, vibrational temperature drops when gas flow (pressure) increases, as confirmed by separate measurements in terms of both vibrational and rotational temperatures. An increment in rotational temperature takes place due to the enhanced number of collisions in the gas at higher flow rates. This suggests that the gas starts losing its vibrational excitation causing a decrease in both the N_2 dissociation, and subsequently the NO formation. In contrast, at low flow rates and pressures, a higher SEI gives a higher electron density, which in turn enhances the

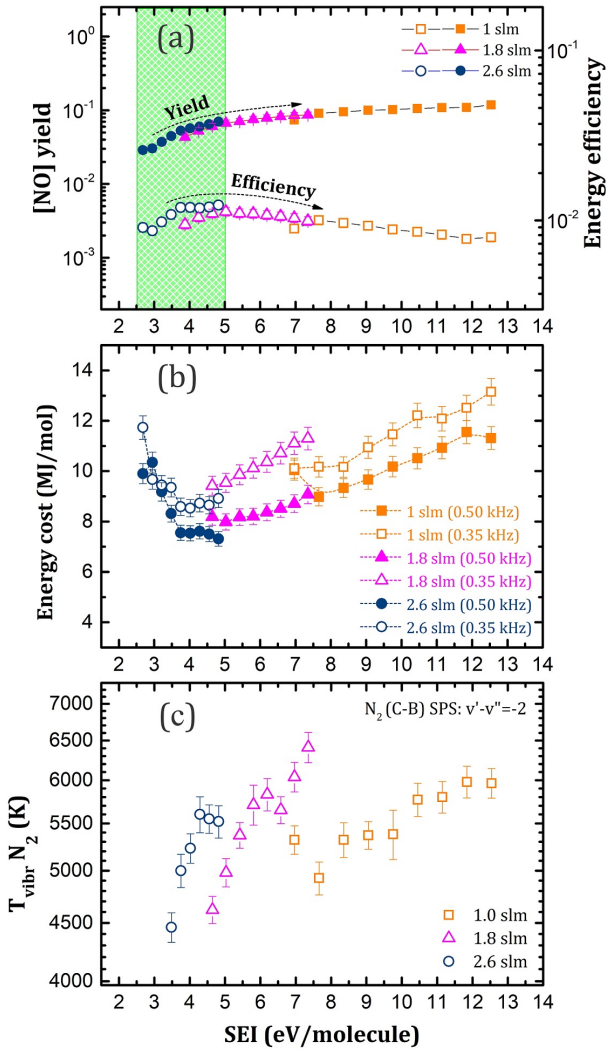

Figure 4. The evolution of (a) the NO yield and energy efficiency, as well as (b) energy cost in the N_2-O_2 pulsed MW discharge as a function of SEI working at three different flow rates of 1, 1.8 and 2.6 slm. (c) The global trend for N_2 vibrational excitation is obtained by tailoring the datasets corresponding to three different gas flows, as a result of system limitations. The typical Boltzmann plot fitting errors are shown as the error bars.

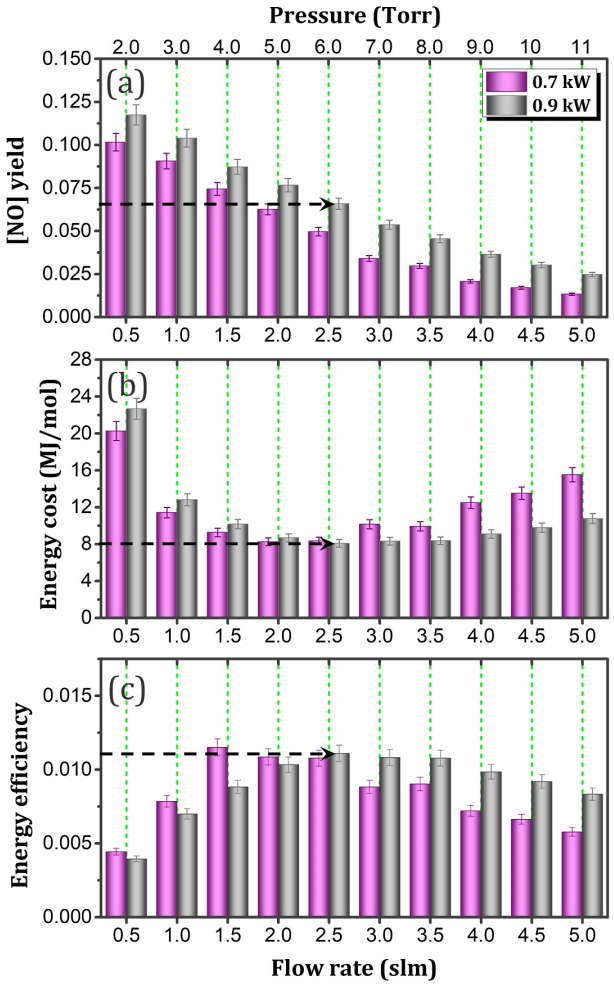

Figure 5. Evolution of the (a) NO yield, (b) energy cost and (c) energy efficiency as a function of the gas flow rate (pressure) measured in the N_2-O_2 pulsed MW discharge at two different applied powers of 0.7 and 0.9 kW. The measurements are taken at a pulse repetition rate of 0.5 kHz with duty ratio of 50%.

vibrational excitation of N_2 by electron impact pathway, as described above.

For better elucidating the linear drop of NO yield at high flow rates, a modelling analysis has been applied. The relative contributions of the two main NO recombination processes at different flow rates are given in Table 5. The recombination reaction (R1) has a contribution larger than reaction (R2). This takes place predominantly due to the two-body recombination reaction between NO and O atoms. It is worth noting that the reaction (R1) is typically not a loss for NO, as NO_2 could react back into NO, while the reactions (R2) and (R3) are real loss processes. Overall, recombination and electron cooling through collisions are the main restrictive factors in reducing NO formation at high flow rates. The reaction balance is further discussed in section 5.4.2 devoted to modelling.

Table 5. Relative contributions of the main recombination mechanisms of NO as a function of the gas flow rate. The entire reactions with respect to both NO formation and recombination processes are not shown here.

Recombination	Contribution[a] (%) at flow rate	
	0.5 slm	5 slm
R1: NO+O ⇒ NO_2	51.2	72.1
R2: N+NO ⇒ O+N_2	27.2	19.6
R3: N(^{2}D)+NO ⇒ O+N_2	9.4	4.0

[a] The sum of contribution is not equal to 100% since only the main recombination reactions are summarized here.

The dependency of the energy cost and efficiency on the flow rate is depicted in Fig. 5(b,c). The lowest energy

cost reaches to 8 MJ/mol with a yield and an energy efficiency of about 7% and about 1%, respectively, in our case. These values were found at a total flow rate of 2.5 slm. This amount also suggests the higher energy efficiency may be achieved at relatively lower flow rates. Therefore, finding an optimum flow rate could be beneficial to improve those values.

5.3. Pulse repetition rate effect. Further optimization of NO production can be obtained by controlling the pulse repetition rate and pulse duration, without increasing the supplied power. Repetitive pulsing not only promotes non-equilibrium conditions in the reactor but also facilitates quenching to produce higher NO_x species [49]. A proper-tuning of plasma frequency could play an important role to improve NO yield.

To study the importance of the power modulation for NO production, we have varied the on- and off-time of the plasma pulse simultaneously, using a constant duty cycle of 50%, while the mean power injected per pulse was kept constant [14]. The experiments were conducted at three different SEI values of 3.75, 6.96 and 9.75 eV/molec. The pulse repetition frequency was varied from 0.1 up to 2 kHz in our case.

The NO production yield reveals a steep growth followed by saturation when pulse repetition frequency increases, as shown in Fig. 6(a). The trend can be explained by a gas residence time (τ_{res}) effect. The τ_{res} is estimated about 2 ms in our case. At low pulse repetition rate (0.1 kHz), pulse duration exceeds τ_{res} and the chance for N_2 and O_2 dissociation remains rather small. In this case, the plasma power is not utilized efficiently since most of the gas passes through the reactor unconverted. The relative portion of the produced NO increases when pulses become more frequent. At intermediate pulses ranging from 0.5 to 0.7 kHz, NO yield values correspond to the optimum case when the pulse duration (about 1.4-2 ms) is close to the τ_{res}. At higher pulse frequencies, however, a small decrease and then a saturation of NO production takes place.

The vibrational and rotational temperatures have been determined based on the time-averaged emission intensity. Both T_{vibr} and T_{rot} decrease simultaneously until pulse repetition rate reaches about 1.0 kHz, as depicted in Fig. 6(b,c). The observed enhancement for f $\geq$ 1.0 kHz could be a result of elevating the V-T transfer at high pulse frequencies provoking the rotational temperature growth (see Fig. 6(c)). Therefore, as we can see, by selecting appropriate values of the pulse duration, the NO yield can be substantially improved. Note that an increase in atomic nitrogen production [63] and CO_2 conversion [24] have been reported in a similar discharge at pulse repetition rates of about 0.75 kHz and 0.5 kHz, respectively.

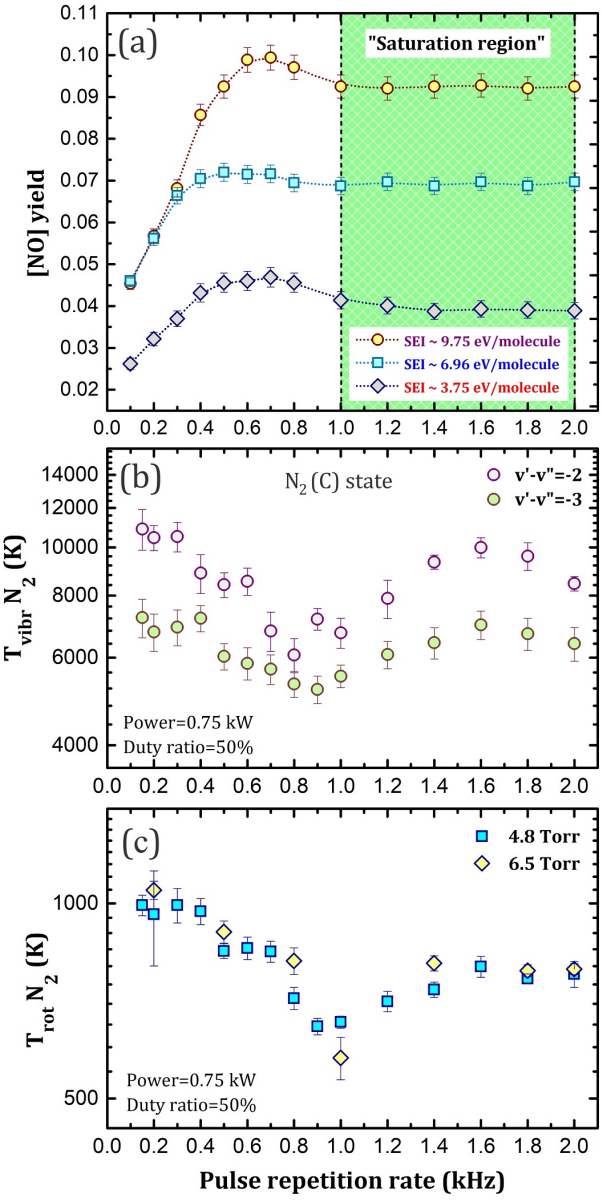

Figure 6. Effect of the pulse repetition rate on (a) the NO yield at three different SEI values of 3.75, 6.96 and 9.75 eV/molec in N_2:O_2 gas mixture, (b) vibrational temperature (T_{vibr}) for the N_2(C) excited state and (c) rotational temperature (T_{rot}) measured in the pulsed MW discharge. Rotational line of the N_2 SPS C-B (0-2) at 385 nm is used for T_{rot} determination. The typical Boltzmann plot fitting errors are shown as the error bars.

5.4. Influence of gas admixture. To investigate the influence of gas admixture on NO production, three different gas mixtures, namely N_2:O_2, N_2:O_2:CO_2 and N_2:CO_2, were used. These experiments were carried out at two different values of SEI, as well as keeping the total flow rate and pulse frequency constant at 1 slm and 0.5 kHz, respectively.

5.4.1. N_2:O_2 gas mixture. The percentage of oxygen in the gas flow plays an important role in the NO_x formation. The NO density produced through the plasma reaction and measured by FTIR is plotted as a function of O_2 flow fraction in N_2 at two different SEI values, as depicted in Fig. 7(a). The N_2/O_2 ratio was varied at a fixed total flow rate of 1 slm and at a fixed pulse repetition rate of 0.5 kHz. A curve with maximum of NO density was achieved by varying O_2 from 10 to 90%. At 50% O_2, the NO density reveals a maximum because the molar balance for reactions (5) and (6) (see above) between N_2 and O_2 takes place under this condition. After the maximum, however, the NO production is decreased owing to the lower amount of N_2 taking part in the discharge. As mentioned earlier, reaction (5) plays a significant role to achieve the higher NO production. Indeed, the high energy required for the reaction between N_2 molecules and O atoms to form NO, can be overcome by the vibrational excitation of N_2. N atoms formed in this process can react with O_2 to form another NO, as given in reaction (6). Based on Zhao *et al.* [64], an increase in O_2 concentration leads to a drop in electron density in N_2-O_2 mixture because of the electronegativity of oxygen. Moreover, a decrease in the nitrogen admixture reduces the atomic nitrogen formation also reducing the NO formation. Indeed, the rate constant of O_2 dissociation by electron collision is almost two orders of magnitude higher [64] than that of N_2 dissociation because oxygen has a lower dissociation energy threshold compared to nitrogen.

In addition, the influence of O_2 admixture on the energy cost of NO formation was also examined. The energy cost keeps decreasing up to 50% of O_2 and has a parabolic trend with a minimum at about 50% of O_2 admixture. The observed trend is a direct consequence of higher NO concentration upon raising the O_2 content (see Fig. 7(c)). A comparison with modelling clarifies additional details in this case, as discussed in the following section.

5.4.2. Reaction analysis for NO formation and recombination. To support the experimental results explained in section 5.4.1, a modelling study was performed in the same conditions as in the experiment. The underlying plasma chemistry, as predicted by the model, for the NO formation and loss/recombination in a N_2-O_2 mixture is discussed here. In the model, the NO density is calculated by balance equations, taking into account the various production and loss terms by different chemical reactions. The calculated trends and values of NO concentration in the N_2-O_2 gas mixture are in rather good agreement with the measured data, as shown in Fig. 7(a,b).

In order to explain the observed trends, the contributions of the relevant kinetic reactions were analyzed. In this case a better insight in the underlying chemical reactions could help to improve the nitrogen fixation. The most important reactions which are responsible for the NO production and recombination are presented in Fig. 8(a). When it comes to production, the reaction between O radicals and vibrationally excited N_2 is of importance contributor below 40% of O_2 content. The dominant formation process of NO corresponds to the contribution of O atoms and NO_2 molecules resulting in forming NO and O_2 molecules for fraction of O_2 above 40%. This can be easily

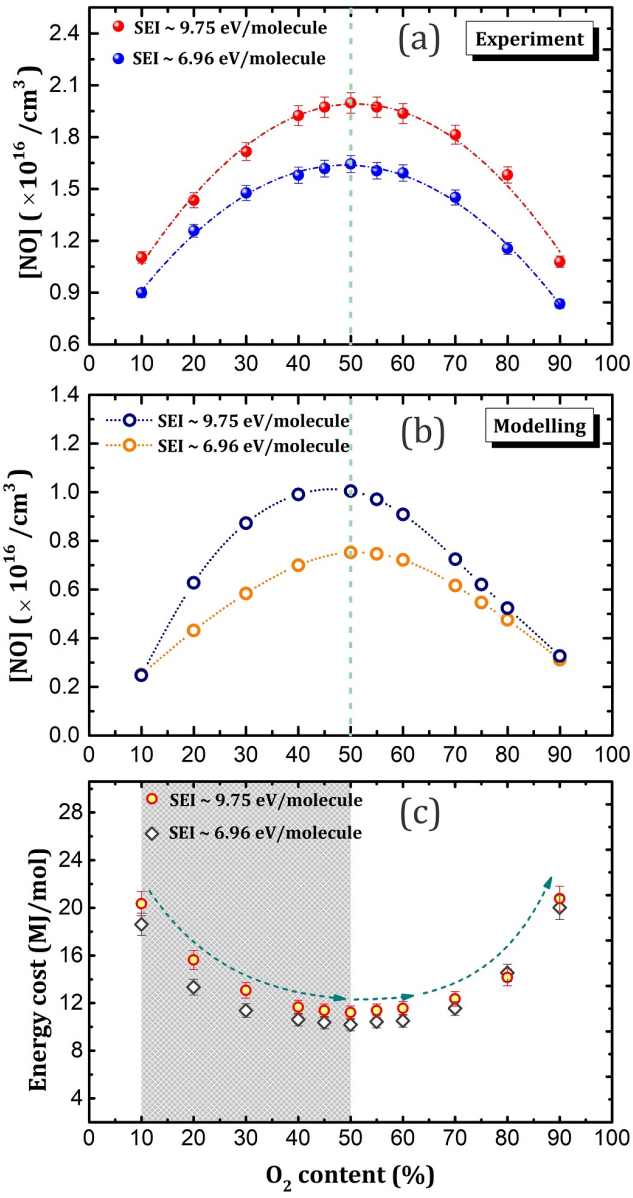

Figure 7. Comparison between the (a) experimental and (b) calculated NO concentration in N_2-O_2 mixture at 6.96 and 9.75 eV/molec as energy inputs, 0.5 kHz as pulse repetition rate with total flow rate of 1 slm. (c) the evolution of energy cost as a function of O_2 content mixed in N_2.

explained by increasing availability of NO_2 (which exists in higher concentrations at high O_2 contents) on one hand, and the lower N_2 concentrations on the other hand. The relative contributions of these reactions are equal at 40% of the O_2 admixture. When looking at the recombination curves, a significant NO loss process is the recombination with O atoms leading to NO_2 through a two-body reaction. Another recombination mechanism taking place at O_2 fractions below 25%, is the reaction of NO with N atoms, yielding the formation of O and N_2. Overall, electron impact dissociation of NO_2 is more important for the formation of NO than the Zeldovich mechanism through vibrational excitation of N_2. This gives us a deeper insight into how the reactions evolve along with an increasing O_2 content.

Vervloessem *et al.* [47] recently demonstrated the role of V-V exchange between N_2 and O_2 in GAP system working at atmospheric pressure. They reported that depopulation of N_2 vibrational levels takes place as a result the V-V exchange between vibrationally excited N_2 and O_2 molecules. In our system, this can be observed for N_2 ($X\ ^1\Sigma_g^+$, v>19), however for N_2 vibrational levels equal to 10 and lower almost no difference can be noticed. We observed as well a slight increase in NO and NO_2 concentrations when N_2-O_2 V-V exchanges are not taken into account. This can be contributed to the fact that the higher N_2 vibrational levels undergo losing their vibrational energy through the N_2-O_2 V-V exchanges in our regular system. As vibrational excitation of N_2 could benefit to overcome the high energy barrier for N_2 dissociation, we measured the vibrational temperature of N_2 molecules as a function of O_2 content, as depicted in Fig. 8(b). A stable growth of T_{vibr} values with the increase of O_2 fraction was found at a fixed SEI value of 9.75 eV/molec in our case. Such an increase could assure the population of higher vibrational energy levels leading to enhanced N_2 dissociation.

Using these data, we can ultimately compose an overall reaction scheme for a better intuition in the underlying chemical reactions, as presented in Fig 9. The width of the arrows is proportional to the reaction rates. For 10% O_2, we find that the most important pathway of NO creation comes from vibrationally excited N_2, with N_2 ($X\ ^1\Sigma_g^+$, v=12) being the biggest contributor. This can be explained by the fact that the 12^{th} vibrational energy level of N_2 has a low energy (about 0.02 eV) required for the NO formation (see reaction (F1)). Interesting to mention that the oxygen atom needed for this reaction is mainly produced by collision with electronically excited N_2 at the beginning of the plasma pulse. The major channels for O-atom formation are as follows in our case:

$$N_2(B^3\Pi_g) + O_2 \longrightarrow N_2 + O + O, (50\%) \qquad (14)$$

$$N_2(A^3\Sigma_u^+) + O_2 \longrightarrow N_2 + O + O, (26\%) \qquad (15)$$

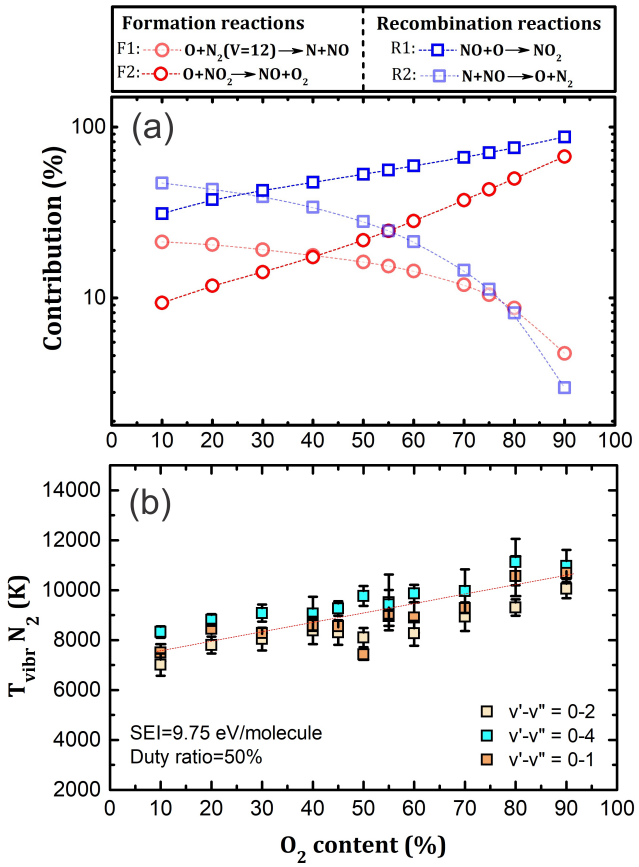

Figure 8. (a) Relative contribution of the main processes leading to NO formation and recombination in a N_2-O_2 mixture as a function of O_2 content at a fixed flow rate of 1 slm and the corresponding SEI of 9.75 eV/molec. (b) T_{vibr} of the N_2(C) excited state measured in the pulsed MW discharge as a function of O_2 fraction in the mixture. Further information regarding the discharge is depicted in the legend. The error bars correspond to the Boltzmann plot fitting error.

$$N_2(a'^1\Sigma_u^-) + O_2 \longrightarrow N_2 + O + O, (11\%) \qquad (16)$$

The main loss contributor is the recombination of NO with N back to N_2. At all admixtures, the most important mechanism for N-atom formation is the electron impact dissociation at the beginning of the plasma on-time and the NO formation reaction, overall. For 50% O_2, the N_2 vibrational pathway (reaction (F1)) is still the biggest contributor for NO production, however, the NO formation from NO_2 (reaction (F2)) becomes increasingly important, afterwards. Notwithstanding, the increase in O_2 promotes formation of NO_2 representing at the same time the biggest loss mechanism for NO. The oxygen atoms are also created by electron impact dissociation in this case. When looking at 90% O_2, it can be observed that the biggest contributor to NO-formation is the creation from NO_2. However, at the same time, the reverse process is also the biggest NO loss mechanism.

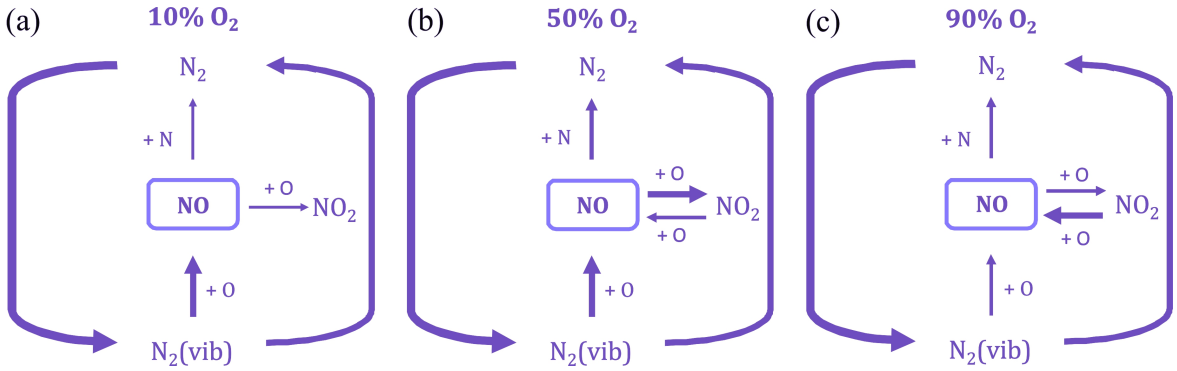

Figure 9. The most important reactions and plasma-chemical mechanisms calculated based on modelling for (a) 10% O_2 (b) 50% O_2 and (c) 90% O_2. A clear vibrational exchange is found between N_2(v=0) and N_2(v>0) states. It can be noticed that with an increasing O_2 concentration the NO_2 pathway becomes more important. The shown arrow thicknesses are proportional to the reaction contribution.

The N_2 vibrational path still accounts for around 20% of the NO-formation.

5.4.3. Other admixtures

CO_2 case. Relative NO and CO densities as a function of CO_2 admixture in N_2 and N_2:O_2 have been investigated in this case at a fixed flow rate of 1 slm and a fixed SEI of 9.75 eV/molec. We observed the formation of CO in the discharge already at a small CO_2 admixture, whereas NO has not been detected up to 30% CO_2 in the mixture, as clearly indicated in Fig. 10(a). On the other hand, a significant growth of CO as well as a slight decrease in NO were also observed in N_2:O_2:CO_2 mixtures (see Fig. 10(b)). The observed trends might be related to the fact that the strong triple CO bond needs a high energy (∼11 eV) to dissociate. The most important electron impact dissociation and excitation reactions in CO_2:N_2 mixture leading to the CO formation are as follows [65, 66]:

$$e^- + CO_2 \longrightarrow CO + O + e^- \quad (17)$$

$$N_2(^1\Sigma_g^+, v) + CO_2 \longrightarrow N_2 + CO + O \quad (18)$$

$$N_2(A^3\Sigma_u^+) + CO_2 \longrightarrow N_2 + CO + O \quad (19)$$

Note that we also suggest that carbon species generated in the discharge may trap oxygen radicals and react with them before N species can combine with oxygen.

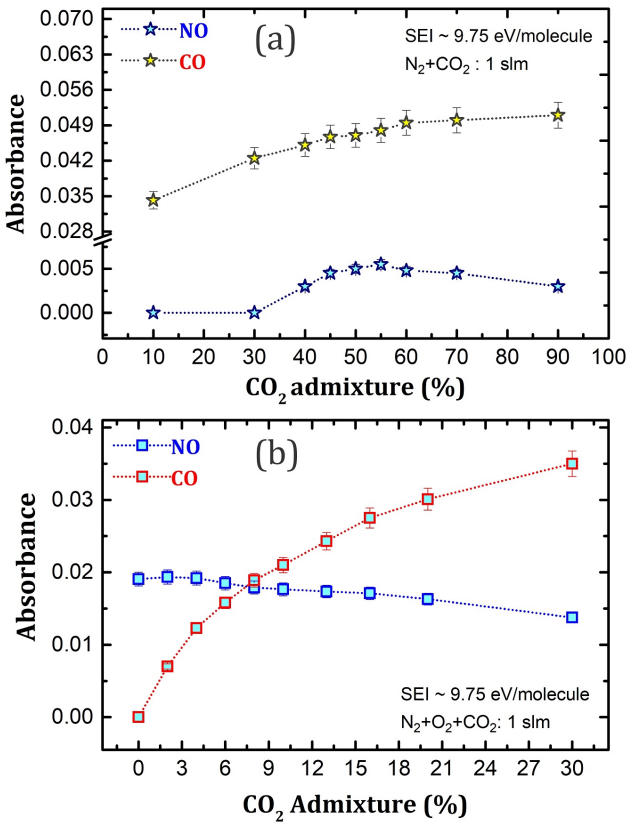

Figure 10. Absorbance of NO and CO species in (a) N_2:CO_2 mixture without O_2 content and (b) N_2:O_2 (1:1) in presence of CO_2 admixture measured at a fixed SEI of 9.75 eV/molec and gas flow rate of 1 slm.

5.5. NO yield and energy cost. In order to benchmark our results with the available studies, we compared the NO yield and energy cost obtained in the present study to other plasma types from literature (see Table 6). The NO yield is considered equal to the NO_x yield since only NO is observed in our case. While our NO yield is quite high, compared to other papers, our energy cost is also quite high, and about one order of magnitude greater than the theoretical limits (0.29 MJ/mol). Indeed, there is often a trade-off between energy cost and yield. In general, however, GAP and MW discharges clearly demonstrate better results in terms of yield and energy cost than the other plasma sources. This is related to the plasma non-equilibrium characteristic for the MW case, promoting

Table 6. Summary of the NO_x yield and energy cost obtained in the literature using different plasma sources operating at atmospheric pressure (unless indicated otherwise).

Reactor	Yield	Energy cost (MJ/mol)	Ref
MW discharge with magnetic field (low pressure)	14% NO	0.29	[49]
Pulsed MW discharge (low pressure)	**~7% NO**	**~8**	**This work**
Pulsed MW discharge (low pressure)	6% NO	0.6	[68]
MW discharge with MoO3 catalyst	6% NO	0.84	[69]
Electric arc (Birkeland-Eyde)	1-2% NO	2.41	[5]
Pulsed milliscale GAP	2% NO_x	2.8	[45, 46]
Plasma arc jet	6.5% NO	4.0	[70]
MW discharge	0.6% NO_x	4.05	[21]
DBD	0.5% NO_x	18	[42]
GAP	1.5% NO_x	3.6	[47]
Spark[a]	-	5.13-8.17	[71]
Propeller Arc[a]	-	3.54-10.58	[71]
DC glow discharge (pin-to-plane)[a]	-	7.15-14.96	[71]
DC glow discharge (pin-to-pin)[a]	-	2.8-3.5	[41]

[a] The energy cost values expressed here in MJ/mol are almost equivalent to those reported by Pei *et al.* [71] in units of GJ/tN (gigajoules expended per metric ton nitrogen produced).

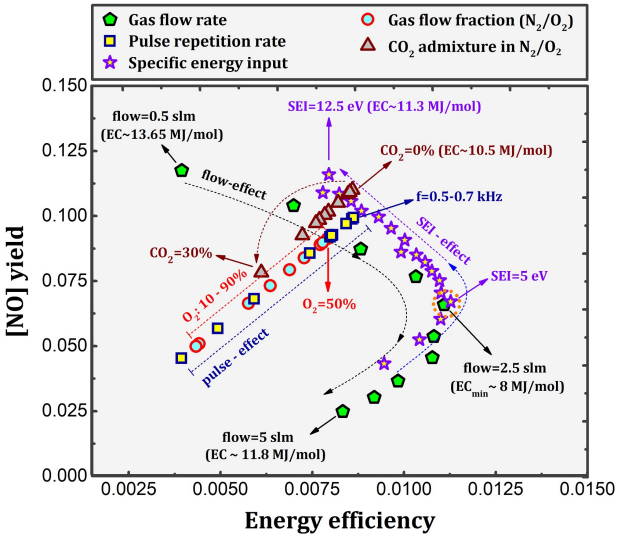

Figure 11. Diagram summarizing the obtained results in the energy efficiency - NO yield coordinates. The effects of gas flow rate (pressure), pulse repetition rate, specific energy input, gas flow fraction and gas admixture are grouped by different colors. EC is defined as energy cost. More information about the discharge condition is available in the legend.

efficient vibrational excitation of molecular nitrogen and thus providing the most energy-efficient N_2 dissociation pathway. The vibrationally excited N_2 molecules, as a result, can significantly enhance the NO synthesis [67]. In terms of industrial scale, the H-B process for ammonia synthesis still has the lowest energy cost of 0.48 MJ/mol. Therefore, major efforts should be placed on NO_x synthesis for non-equilibrium plasma-based N_2 fixation to further increase the yield and decrease the energy cost. We suggest a better performance toward nitrogen fixation in MW discharges could be achieved by further tuning of the MW discharge properties at low pressure.

6. Conclusions and perspectives

In this work we demonstrated the capabilities of a pulsed microwave discharge for the NO production in different gas mixtures by means of infrared absorption and emission spectroscopy, as well as using modelling. We have shown that the lowest energy cost obtained as a result of optimization of plasma parameters reaches value of 8 MJ/mol with a yield and an energy efficiency of about 7% and 1%, respectively. Based on a comparison with modelling, we attribute this result to vibrational excitation of N_2 related to the non-equilibrium MW discharge. Our experimental results also show that the NO production can be enhanced additionally by tuning the discharge pulse repetition rate, which primarily related to the gas residence time in our case. The measurements demonstrate that higher pressure have a negative effect on NO production yield, while a lower pressure (associated with a higher SEI value) is beneficial, as it supports vibrational excitation of the involved molecules. These trends are additionally supported by kinetic plasma modelling showing the decisive role of both the vibrational excitation of N_2 and O_2 as well as the electron impact excitation in molecular dissociation and consequent NO formation.

The main obtained trends in terms of NO yield and energy efficiency that have been acquired experimentally are summarized in Fig. 11. The higher NO yield is obtained at lower gas flow (0.5 slm), while the energy efficiency maximizes at gas flow rate of about 2.5 slm (corresponded to the lowest energy cost), thereafter, it decreases gradually. A clear decrease in both NO yield and energy efficiency is observed upon adding CO_2 gas (triangles in Fig. 11). The decrease in NO yield at higher gas flow (pressure) takes place in case when SEI decreases. The optimal pulse repetition rate with respect to the NO yield and energy efficiency is found between 0.5-0.7 kHz with duty ratio of 50% (yellow rectangles in Fig. 11). This is related to the case when pulse duration (between 1.4-2 ms) is close to the gas residence time (estimated about 2 ms). A clear increase in NO yield and a decrease in energy efficiency are found when SEI exceeds 5

eV (violet star symbols in Fig. 11). In case of O_2 flow fractions mixed in N_2 (circle symbols), the higher yield is acquired in a balance ratio of N_2:O_2 (1:1), as verified by reaction analysis predicted by plasma modelling in terms of NO formation and recombination processes. Our model results show that the reactions $O+N_2(X\,^1\Sigma_g^+, v=12)\Rightarrow NO+N$ and $NO_2+O\Rightarrow NO+O_2$ are mainly contribute for NO formation, whereas the reactions $NO+O\Rightarrow NO_2$ and $NO+N\Rightarrow N_2+O$ are responsible for recombinaiton processes.

Application of power-modulated low-pressure MW discharges may be promising at the industrial scale when both NO_x yield and the corresponding energy cost should be optimized. Strategies which could be proposed for further understanding of NO formation mechanisms in the pulsed MW discharge may include:
- Extended post-discharge studies involving gas temperature measurements.
- Better clarification of NO formation mechanism by in-situ FTIR studies in the discharge region.
- Cross-checking the obtained trends in the discharge region using laser spectroscopy with higher temporal and special resolution.

Acknowledgements

The research is kindly supported by the FNRS-FWO project NITROPLASM, EOS O005118F. O. Samadi also acknowledges PhD student F.Manaigo for cooperation in doing the additional measurements.

Appendix. Zero-Dimensional Plasma Kinetics solver

The ZDPlasKin code [47] allows us to calculate the changes in densities of the species, as well as the gas temperature in function of time. This is done by solving the mass conservation equation for every species, the Boltzmann equation and the gas thermal balance. The mass conservation equation for every species is written as follows:

$$\frac{dn_s}{dt} = \sum_{j=1}^{j_{max}} Q_{sj} = \sum_{j=1}^{j_{max}} R_j[a_{sj}^R - a_{sj}^L], R_j = k_j \prod_l n_l, \tag{20}$$

where n_s is the density of the species s, Q_{sj} is the source term for reaction j of the species s, a_{sj}^R and a_{sj}^L represent the stoichiometric coefficients on the right and left side, respectively, of species s for reaction j. R_j is the reaction rate and k_j the reaction rate coefficient.

For the electrons, BOLSIG+ solves the Boltzmann equation for the given reduced electric field, through the provided electron impact reactions and the corresponding cross-sections. As a result the electron density distribution function (EEDF) can be obtained. This allows us to use the mean electron energy in the calculations of the electron energy, and therefore the electron temperatures. The needed reduced electric field is calculated from Joule heating:

$$\frac{dP}{dV} = JE = \sigma E^2 \tag{21}$$

where P is the power and dV a volume element, $J=\sigma E$ is the current density and $\sigma = en_e\mu_e$ is the electron conductivity. The reduced field is represented by E/N, with N the total density of gas-phase species, p=P/V the power density, n_e the electron density and e the electron charge, as given:

$$\frac{E}{N} = \frac{1}{N}\sqrt{\frac{p}{\sigma}} \tag{22}$$

The power density is defined by the power input P and position along the axis in the plasma, as well as by the length L of the plasma and the radius r of the tube. The power density follows a triangular shape in the plasma along the tube with the middle of the plasma (where the waveguide is) a maximum power density (p_{max}). After this maximum, the power density is decreased again until the end of the plasma, after which an afterglow will take place. The power density maximum is defined as:

$$p_{max} = \frac{2P}{L\pi r^2} \tag{23}$$

During the calculations, the mass flow rate and pressure are taken constant. Hence, the species densities are adapted to keep the mass flow rate and pressure constant. The gas flow velocity in the tube is calculated based on the known flow rate (Q_m), the cross-section area (A) and the mass density (ρ^*) calculated for each species s from the number density n and the mass M using the expression:

$$v = \frac{Q_m}{\rho^* A} = \frac{Q_m}{\sum_s n_s M_{s^*} \pi R^2} \tag{24}$$

References

[1] United Nations Environment Programme and Woods Hole Research Center 2007 *United Nations Environ. Program.* 1–56
[2] Graham P H and Vance C P 2000 *F. Crop. Res.* **65** 93–106
[3] Wang W, Patil B, Heijkers S, Hessel V and Bogaerts A 2017 *ChemSusChem* **10** 2145–2157
[4] Cherkasov N, Ibhadon A O and Fitzpatrick P 2015 *Chem. Eng. Process. Process Intensif.* **90** 24–33
[5] KR BIRKELAND 1906 *Trans. Faraday Soc.* **2** 98–116
[6] Erisman J W, Sutton M A, Galloway J, Klimont Z and Winiwarter W 2008 *Nat. Geosci.* **1** 636–639
[7] Peng P, Schiappacasse C, Zhou N, Addy M, Cheng Y, Zhang Y, Ding K, Wang Y, Chen P and Ruan R 2019 *ChemSusChem* **12** 3702–3712

[8] He Y, Chen Z, Li Z, Niu G and Tang J 2018 *Front. Optoelectron.* **11** 92–96

[9] Patil B S, Wang Q, Hessel V and Lang J 2015 *Catal. Today* **256** 49–66

[10] Fridman A 2008 *Plasma chemistry* (Cambridge university press)

[11] Li S, Medrano J A, Hessel V and Gallucci F 2018 *Processes* **6**

[12] Anastasopoulou A, Wang Q, Hessel V and Lang J 2014 *Processes* **2** 694–710

[13] Moisan M, Chaker M, Zakrzewski Z and Paraszczak J 1987 *J. Phys. E.* **20** 1356–1361

[14] Silva T, Britun N, Godfroid T, Van Der Mullen J and Snyders R 2016 *J. Appl. Phys.* **119**

[15] Britun N, Godfroid T and Snyders R 2020 *J. CO2 Util.* **41** 101239

[16] Rusanov V D, Fridman A A and Sholin G V 1981 *Sov. Phys. Uspekhi* **24** 447–474

[17] Baeva M, Gier H, Pott A, Uhlenbusch J, Höschele J and Steinwandel J 2002 *Plasma Chem. Plasma Process.* **22** 197

[18] Britun N and Hnilica J 2020 *J. Appl. Phys.* **127** 211101

[19] Na Y H, Kumar N, Kang M H, Cho G S, Choi E H, Park G and Uhm H S 2015 *J. Phys. D. Appl. Phys.* **48** 1–7

[20] Lee J, Sun H, Im S K and Soo Bak M 2017 *J. Appl. Phys.* **122**

[21] Kim T, Song S, Kim J and Iwasaki R 2010 *Jpn. J. Appl. Phys.* **49**

[22] Asisov R I, Givotov V K, Krasheninnikov E G, Potapkin B V, Rusanov V D and Fridman A 1983 Carbon Dioxide Dissociation in Non-Equilibrium Plasma *Sov. Phys. Dokl* vol 271 p 94

[23] Berthelot A and Bogaerts A 2017 *J. Phys. Chem. C* **121** 8236–8251

[24] Britun N, Silva T, Chen G, Godfroid T, Van Der Mullen J and Snyders R 2018 *Plasma-assisted CO2 conversion: Optimizing performance via microwave power modulation* vol 51

[25] Vermeiren V and Bogaerts A 2019 *J. Phys. Chem. C* **123** 17650–17665

[26] Jivotov V 1998 *J. Phys. IV JP* **8**

[27] Van Alphen S, Vermeiren V, Butterworth T, Van Den Bekerom D C, Van Rooij G J and Bogaerts A 2020 *J. Phys. Chem. C* **124** 1765–1779

[28] Fantz U 2006 *Plasma Sources Sci. Technol.* **15**

[29] Zhu X M and Pu Y K 2010 *J. Phys. D. Appl. Phys.* **43**

[30] Bruggeman P J, Sadeghi N, Schram D C and Linss V 2014 *Plasma Sources Sci. Technol.* **23**

[31] Britun N, Palmucci M, Konstantinidis S, Snyders and Rony 2012 *IOP Conf. Ser. Mater. Sci. Eng.* **39**

[32] Britun N, Minea T, Konstantinidis S and Snyders R 2014 *J. Phys. D. Appl. Phys.* **47**

[33] Engeln R, Klarenaar B and Guaitella O 2020 *Plasma Sources Sci. Technol.* **29**

[34] Klarenaar B L M, Engeln R, Van Den Bekerom D C M, Van De Sanden M C M, Morillo-Candas A S and Guaitella O 2017 *Plasma Sources Sci. Technol.* **26** 115008

[35] Liu Y, Welzel S, Starostin S A, Van De Sanden M C M, Engeln R and De Vries H W 2017 *J. Appl. Phys.* **121**

[36] Sansonnens L, Howling A A and Hollenstein C 1998 *Plasma Sources Sci. Technol.* **7** 114–118

[37] Nair S A, Nozaki T and Okazaki K 2007 *Ind. Eng. Chem. Res.* **46** 3486–3496

[38] Raynaud P, Marlière C, Berthomieux D, Segui Y, Durand J and Burke R 1998 *J. Phys. IV JP* **8** 285–291

[39] Xu S, Khalaf P I, Martin P A and Christopher Whitehead J 2018 *Plasma Sources Sci. Technol.* **27**

[40] Sremački I, Gromov M, Leys C, Morent R, Snyders R and Nikiforov A 2019 *Plasma Process. Polym.* 1–12

[41] Pei X, Gidon D and Graves D B 2020 *J. Phys. D. Appl. Phys.* **53**

[42] Patil B S, Cherkasov N, Lang J, Ibhadon A O, Hessel V and Wang Q 2016 *Appl. Catal. B Environ.* **194** 123–133

[43] Tang X, Wang J, Yi H, Zhao S, Gao F and Chu C 2018 *Plasma Chem. Plasma Process.* **38** 485–501

[44] Pipa A V, Bindemann T, Foest R, Kindel E, Röpcke J and Weltmann K D 2008 *J. Phys. D. Appl. Phys.* **41**

[45] Patil B S, Rovira Palau J, Hessel V, Lang J and Wang Q 2016 *Plasma Chem. Plasma Process.* **36** 241–257

[46] Patil B S, Peeters F J J, van Rooij G J, Medrano J A, Gallucci F, Lang J, Wang Q and Hessel V 2018 *AIChE J.* **64** 526–537

[47] Vervloessem E, Aghaei M, Jardali F, Hafezkhiabani N and Bogaerts A 2020 *ACS Sustain. Chem. Eng.* **8** 9711–9720

[48] Tang J, Zhang T, Liang D, Xu C, Sun X and Lin L 2000 *Chem. Commun.* **1** 1861–1862

[49] Asisov R, Givotov V, Rusanov V and Fridman A 1980 *Sov. Phys.* **14** 366 (*Preprint* `Asisov`)

[50] Wandell R J, Wang H, Bulusu R K, Gallan R O and Locke B R 2019 *Plasma Chem. Plasma Process.*

[51] Chen G, Britun N, Godfroid T, Georgieva V, Snyders R and Delplancke-Ogletree M P 2017 *An overview of CO2 conversion in a microwave discharge: The role of plasma-catalysis* vol 50

[52] Silva T, Britun N, Godfroid T and Snyders R 2014 *Plasma Sources Sci. Technol.* **23**

[53] Chen G, Silva T, Georgieva V, Godfroid T, Britun N, Snyders R and Delplancke-Ogletree M P 2015 *Int. J. Hydrogen Energy* **40** 3789–3796

[54] Christensen P A, Ali A H B M, Mashhadani Z T A W and Martin P A 2018 *Plasma Chem. Plasma Process.* **38** 293–310

[55] Pancheshnyi S, Eismann B, Hagelaar G J M and Pitchford L C 2008 *Univ. Toulouse, LAPLACE, CNRS-UPS-INP, Toulouse, Fr.*

[56] Goldman A, Brown L R, Schoenfeld W G, Spencer M N, Chackerian C, Giver L P, Dothe H, Rinsland C P, Coudert L H, Dana V and Mandin J Y 1998 *J. Quant. Spectrosc. Radiat. Transf.* **60** 825–838

[57] Thompson H W and Green B A 1956 *Spectrochim. Acta* **8** 129–137

[58] Ballard J, Johnston W B, Kerridge B J and Remedios J J 1988 *J. Mol. Spectrosc.* **127** 70–82

[59] Rothman L S, Gordon I E, Babikov Y and Barbe A 2013 *J. Quant. Spectrosc. Radiat. Transf. Radiat. Transf.* **130** 4–50

[60] Rank D H, Skorinko G, Eastman D P and Wiggins T A 1960 *J. Mol. Spectrosc.* **4** 518–533

[61] Mantz A W and Maillard J P 1974 *J. Mol. Spectrosc.* **53** 466–478

[62] Suzuki I 1968 *J. Mol. Spectrosc.* **25** 479–500

[63] Godfroid T, Dauchot J P and Hecq M 2005 *Surf. Coatings Technol.* **200** 649–654

[64] Zhao G B, Garikipati S V, Hu X, Argyle M D and Radosz M 2005 *AIChE J.* **51** 1800–1812

[65] Snoeckx R, Heijkers S, Van Wesenbeeck K, Lenaerts S and Bogaerts A 2016 *Energy Environ. Sci.* **9** 999–1011

[66] Ramakers M, Heijkers S, Tytgat T, Lenaerts S and Bogaerts A 2019 *J. CO2 Util.* **33** 121–130

[67] Bogaerts A and Neyts E C 2018 *ACS Energy Lett.* **3** 1013–1027

[68] Polak, L S; Ovsiannikov, A A; Slovetsky, D I; Vurzel F B 1975 *Nauk.* Moscow

[69] Mutel B, Dessaux O and Goudmand P 1984 *Rev. Phys. Appliquée* **19** 461–464

[70] Namihira T, Katsuki S, Hackam R, Akiyama H and Okamoto K 2002 **30** 1993–1998

[71] Pei X, Gidon D, Yang Y J, Xiong Z and Graves D B 2019 *Chem. Eng. J.* **362** 217–228